SCIENCE CHINA
Technological Sciences

• Article •

May 2014 Vol.57 No.5: 953–961
doi: 10.1007/s11431-014-5513-5

Local porosity distribution of cement paste characterized by X-ray micro-tomography

WAN KeShu[1,2*] & XU Qiong[2]

[1] *Jiangsu Key Laboratory of Construction Materials, Nanjing 211189, China;*
[2] *School of Materials Science and Engineering, Southeast University, Nanjing 211189, China*

Received September 27, 2013; accepted December 27, 2013

Porosity is one of the most important parameters for cement-based materials, which influences the mechanical property, transport property, and durability. The spatial and frequency distributions of local porosity of cement pastes are characterized using X-ray micro-tomography data and treating methods. The 3D spatial distributions for three cement paste specimens with different water cement (w/c) ratios show reasonable heterogeneity. The probability analysis also reveals this heterogeneity: the representative volume element (RVE) size based on porosity maps decreases with w/c ratio firstly, then increases with w/c ratio; and the heterogeneity on the characterized probe size or on the RVE size increases with w/c ratio. Average porosities obtained using the CT method are further compared with those by traditional methods.

cement-based materials, local porosity, spatial distribution, porosity probability, tomography

Citation: Wan K S, Xu Q. Local porosity distribution of cement paste characterized by X-ray micro-tomography. Sci China Tech Sci, 2014, 57: 953–961, doi: 10.1007/s11431-014-5513-5

1 Introduction

The ability to characterize microstructure is important for material science, because microstructure is one of the most important parameters which affect material performance. For the cement-based materials, the pore structures play a crucial role in the mechanical property, transport property, and durability of this kind of material. As one of the most important parameters of pore structure, porosity is defined as the ratio of the volume of empty space to the total volume of the porous materials and is in a range from 0 to 1 [1]. How to correctly characterize the porosity and porosity distribution is a challenge.

Two kinds of tools are generally applied to characterize this parameter; one is for quantitative evaluation and the other is for observation. Gravimetric method, mercury intrusion porosimetry (MIP), and absorption method BET, etc. are widely used to quantitatively characterize the porosity of the cement-based materials [2–4], while all of these methods can only give the average porosity information of the whole characterized sample without spatial resolution showing the heterogeneity information.

For observation methods, scanning electron microscopy (SEM) and optical microscopy are widely applied to characterize the porosity of the materials through statically calculating the pore area within a typical sectional 2D surface [5,6]. One challenge in using 2D sectional surface is the damage arising in sample preparation processes, which needs to be carefully controlled in the cutting and polishing processes, and the other problem is that the 2D information is not enough for 3D microstructure. The recently developed focused ion beam (FIB) tomography overcomes the manual difficulty. This technique involves the steps of milling serial cross-sections through a surface by FIB, imaging

*Corresponding author (email: keshuwan@seu.edu.cn)

each sequential 2D section typically by secondary electrons (SE), and then aligning the 2D images of the sectioned material to visualize the 3D microstructure using a specialized software. The method has been applied to characterize the pore space of the cement-based materials [7–9]. However, the complicated imaging process, the damage in sample preparing and in imaging, and small field of view have limited its further applications in the cement-based materials.

X-ray computer tomography (CT) can observe the 3D pore space directly without sample preparation and damage, and the porosity can be simply calculated by image segmentation techniques [10–14]. While two problems limit its applications to porosity determination. Firstly, spatial resolution for micro-pore is still not sufficient even using the synchrotron micro-tomography with highest spatial resolution, so that the porosity is greatly underestimated [13,14]. Secondly, because of the nature of the CT image and the sensibility of image segmentation techniques [15], there is a large uncertainty in the determined porosity [15,16].

In the pioneer work of Withjack [17], the method of calculating porosity by dual CT scans obtained with different fluids saturating the porous medium was established. Akin et al. [18] proposed a similar method employing a dual scan at two energy levels. These methods using dual CT scans were reviewed by Akin and Kovscek [19]. The dual scan methods are mainly applied in hospital tomography apparatus. To further improve the spatial resolution, one reasonable method is to apply the method in micro CT apparatus, but it is not so straightforward. To overcome the difficulty of *in-situ* saturation in micro CT systems, Ketcham et al. [20] combined *ex-situ* saturation and imaging registration method to obtain the porosity distribution of rock samples. Wan et al. [21] investigated the macro porosity distribution of partly calcium leached cement pastes using the *ex-situ* saturation and imaging registration method.

Considering the heterogeneity of the cement-based materials and rocks, the porosity depends on the analyzed position and size, so how to evaluate the porosity distribution is significant. Hilfer [22] and Biswa et al. [23] proposed a local porosity theory (LPT) for rocks, where he considered the porosity itself as the random variable, and the fluctuations in porosity as well as in connectivity were investigated. The theory was used by Hu et al. [24] to assess the porosity heterogeneity of cement paste with different age and water cement (w/c) ratios. While the 2D SEM image applied in their research [24] was an indirect method for 3D porosity, which would inevitably introduce some errors.

In this research, the spatial porosity distribution of cement pastes is characterized by the dual CT scan method with one CT on dry specimen and the other on saturated specimen. And the probability of porosity is further analyzed from the spatial porosity distribution. The average results are compared with gravimetric results and MIP results. The objective of the current research is to measure the local porosity probabilities of cement pastes with different w/c ratios, thereby providing 3D geometric characteristics of the cement-based materials.

2 Material and method

2.1 Material

The specimens were prepared with PI 52.5 Portland cement from Wuhan Huaxin factory, which were produced by mixing the pure cement clinker with 5 wt% gypsum. The chemical compositions of cement are listed in Table 1. Polycarboxylicacid superlasticizer from Jiangsu Construction Science Research Institute was applied to the w/c ratio 0.35 and 0.23 samples, whose water reducing ratio is over 25%. Three w/c ratios were considered in this research, and the noted names of the specimens and the mix proportions are presented in Table 2. All the specimens were cured in a standard curing room (temperature 20°C±3°C, relative humidity over 95%) for 30 months. The size of the cast prismatic specimen was 40 mm×40 mm×160 mm. To shorten the time for drying and saturation, only a thin plate with size of 40 mm×40 mm×3 mm was cut for further experiments.

2.2 Dual CT scanning method to determine 3D local porosity map

The principle of X-ray CT imaging has been discussed extensively elsewhere [21,25–27]. The resulting CT image is a spatial distribution of the linear attenuation coefficients, which is expressed by grayscale values (GSV) or CT numbers, with brighter regions corresponding to higher values of the linear attenuation coefficient and darker regions to lower ones.

The dual CT scanning method is mainly based on the partial volume effect or the additivity rule of linear attenuation coefficient. Detailed principle and description of the method can be found elsewhere [17–21]. In summary, local porosity of each voxel, ϕ, can be obtained by

$$\phi = \frac{\mu_s - \mu_d}{\mu_w - \mu_a}, \tag{1}$$

where μ_s and μ_d are the linear attenuation coefficients of the voxel of the sample in the saturated state and in dry state

Table 1 Chemical composition of the cement (wt%)

CaO	SiO_2	Al_2O_3	Fe_2O_3	MgO	SO_3	K_2O	Na_2O	Others[a)]	LOI	Total
62.60	21.35	4.64	3.31	3.08	2.25	0.54	0.21	1.07	0.95	100.00

a) Others include TiO_2, P_2O_5, BaO, ZnO, MnO, SrO, PbO, and Cl.

Table 2 Mix proportions of the cement paste specimens

Specimen	Cement	Water	Water reducing admixture
P53	1	0.53	0
P35	1	0.35	0.008
P23	1	0.23	0.016

respectively; μ_d and μ_a are the linear attenuation coefficients of water and air respectively. If two CT scans are taken at identical geometrical positions and scanning conditions, the local porosity distribution can be expressed by

$$\phi = \frac{G_s - G_d}{G_w - G_a}, \tag{2}$$

where G_s and G_d are the GSV of the voxel of the sample in the saturated state and in dry state respectively, G_w and G_a are the GSV of water and air respectively.

Considering eqs. (1) and (2) stand for any voxel or volume, let us define a local cell of $K(x, y, z, l)$, where x, y, and z are the geometrical coordinates, and l is the spatial resolution of the CT scan, then the local porosity of $K(x, y, z, l)$ cell can be expressed by

$$\phi(x, y, z, l) = \frac{G_s(x, y, z) - G_d(x, y, z)}{G_w - G_a}. \tag{3}$$

So, if two CT scans, one in dry state and the other in the saturated state, are taken on the same specimen at identical geometrical positions and scanning conditions, the local porosity distribution can be experimentally determined.

It is very hard to keep the two CT scans with the same geometrical position, so that eq. (3) cannot be applied directly. Therefore 3D image registration process [20,21,28] was applied on the CT data sets. After the 3D image registration, eq. (3) can be applied to calculate the porosity distribution using the CT data of the dual scans.

2.3 Methods to determine the local porosity probability on 3D porosity map

LPT was originally introduced as a quantitative substitute for pore size distributions [22,23]. The idea is to measure porosity or other well-defined geometric observables within a bounded (compact) subset of the porous medium and to collect these measurements into various histograms (probability densities). LPT encompasses two geometric characteristics, i.e., local porosity probability and local percolation probability. Only local porosity probability is considered in this research.

The local porosity at position (x, y, z) and with a cell volume of L^3 was denoted as $\phi(x, y, z, L)$, and the relation between l and L is integral times, which means that the small cells of linear dimension l (voxel size) can be merged into large cell of linear dimension L. Different from the calculating process in the original LPT, the porosity map is experimentally obtained using the dual CT method introduced in Section 2.2. Accordingly, different from the calculation method in the original LPT, the local porosity probability $\mu(\phi, L)$ can be directly expressed by the histogram of digital image of $\phi(x, y, z, L)$ in this research.

Because both $\phi(x, y, z, L)$ and $\mu(\phi, L)$ depend on L, how to select the proper size L is extremely important. As is clear that the smallest L is l, the largest L is the specimen size. Representative volume element (RVE) has been intensively applied to transport or mechanical properties research of the cement-based materials [24,29,30]. RVE can be defined on different structures or properties, and different definitions give different RVE sizes. In this research, the pore structure or local porosity information is applied to the RVE definition, and the RVE size is determined using the average porosity method. Firstly, select a random point, and the cell (with size of L^3) around the point grows larger and larger; secondly, the curve between the average porosities on different cell sizes and the L size is obtained; thirdly, when the curve becomes flat, the L size is defined as the RVE size.

Once the RVE sizes for different specimens are determined, the local porosity probability of the different specimens can be compared on the RVE size. According to the physical meaning of RVE, most of the information of porosity distribution has been removed on the RVE size, so a smaller size is hoped for tacking the statistical porosity fluctuations. Of course, using the smallest probe size of l is a direct way, while it is unfair to compare the different specimens with different RVE size by using the same probe size. Thus, a characterized size is selected by taking the ratio of the RVE size and L size constant for different specimens. In this research, the local porosity probabilities of the different specimens are compared on three different probe sizes, including the RVE size, the smallest probe size, and the characterized size.

2.4 X-ray CT scans and *ex situ* saturation

For the dual CT scans, the specimens were firstly dried in a vacuum oven at 50°C until the weight was stable. This stage lasted for 15 days for the specimen with thickness of about 3 mm. The dry sample was fixed to the rotation stage of CT apparatus, and then scanned, and the reconstructed CT image was hereinafter referred to as the "dry" data. The same specimen was removed from the CT apparatus and immersed into water and vacuum saturated for 7 days until the weight was stable, then the sample was taken out for the second CT scan, and the reconstructed CT image was hereinafter referred to as the "saturated" data.

All the CT scans were performed at the YXLON microfocus X-ray CT system (Y.CT Precision S, YXLON). The X-ray source is 225 kV twin head microfocus source

(Y.FXE 225.99), with direct beam head and transmission beam head. For the direct beam head used in this research, the focus spot size is capable of less than 3 μm. The detector is a flat panel detector (Y.XRD 0820) with pixel number of 1024×1024 and pixel size of 200 μm. All the scans were performed with the same parameters of X-ray peak energy at 195 kV, current at 0.3 mA. And the magnification was 3.3 times so that the effective pixel and voxel size was 60 μm. Each scan consisted of 1080 projections, with an acquisition time of 2 s per projection.

2.5 Gravimetric method for average porosity testing

The average porosity can be estimated by filling the pores with water and determining their volume from the mass difference between the dry specimen and the water saturated specimen. And according to Archimedes' principles, the average porosity can be calculated by three measurements of the mass of the porous specimens, using the following equation:

$$\phi = \frac{m_s - m_d}{m_s - m_{ss}}, \tag{4}$$

where m_s is the mass of the water saturated specimen, m_d is the mass of the dry specimen, m_{ss} is the submerged mass of the saturated specimen in water. The drying and saturation processes are the same as that in Section 2.4.

2.6 Mercury intrusion porosimetry (MIP) testing

The MIP tests were performed with Micrometrics AutoPore IV 9500, whose maximum pressure can be up to 415 MPa and the determined pore size is in the range of 3 nm to 360 μm. The measurement was conducted in two stages: a manual low pressure ranged from 0.003 to 0.21 MPa and an automated high pressure from 0.21 to 242 MPa, and the determined pore size was in the range of 6 nm to 360 μm. After the low-pressure testing, the penetrometer was removed and weighted. Then the high-pressure testing was initiated. The machine was set to equilibrate 10 s and contact

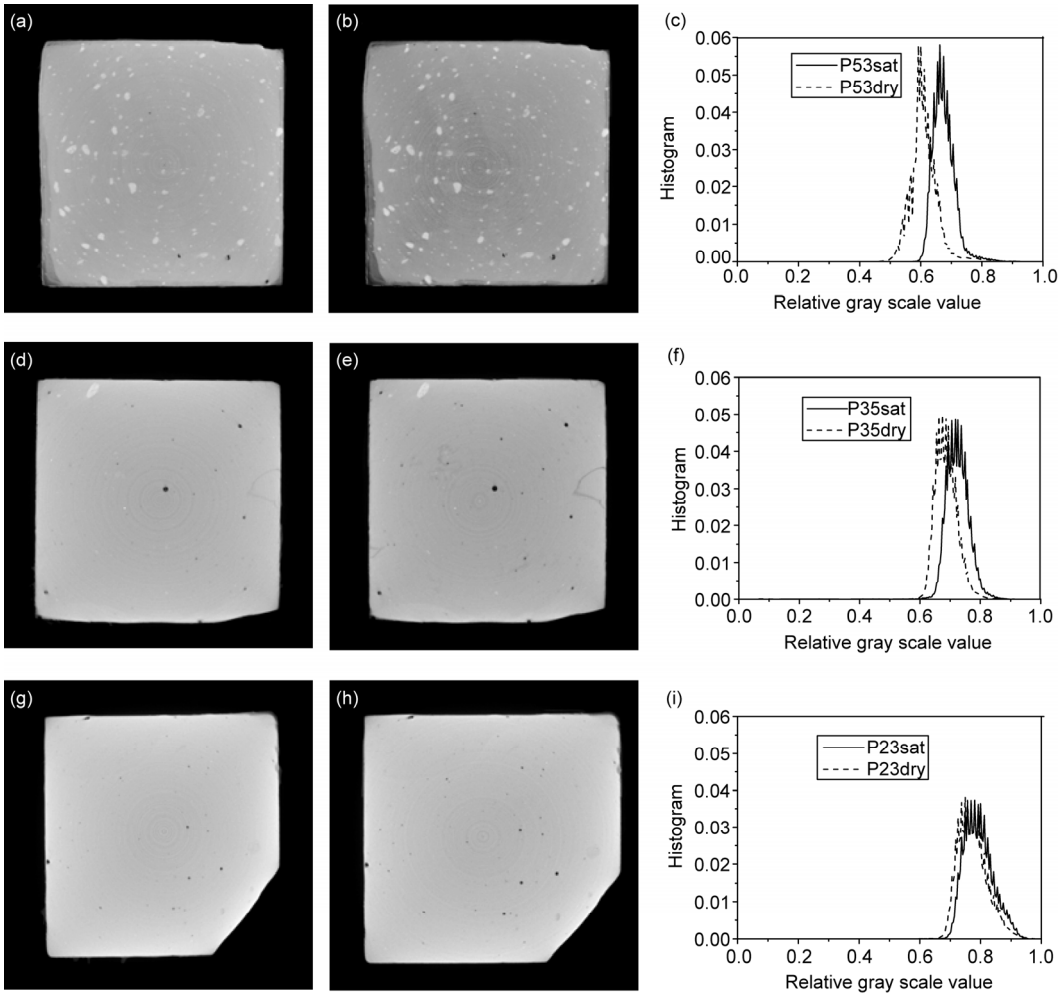

Figure 1 Raw CT data of different specimens. (a), (d), (g) typical 2D slices of the saturated specimens P53, P35, P23, respectively; (b), (e), (h) typical 2D slices of the dry specimens P53, P35, P23, respectively; (c), (h), (i) histograms of (a) and (b), (d) and (e), (g) and (h), respectively.

angle of 130°.

3 Results and discussion

3.1 Raw CT data

To compare the different CT data sets, all the GSV of the CT images were normalized using the same standard. Figure 1 shows the raw CT results of the specimens in dry state and in saturated state, some information can be obtained directly. Firstly, the difference of GSV between the dry specimen and saturated specimen can be clearly distinguished from the histograms, and it is the GSV difference that is applied to porosity characterization in this research. Secondly, the GSV difference is large for specimen with high w/c ratio, and vice versa, which implies the porosity increase with the w/c ratio. Thirdly, the influence of the w/c ratios on GSV can be distinguished: high w/c ratio corresponds to low GSV and the converse is also true.

3.2 Image registration

Figure 2 shows the image registration results using example slices of P35 specimen. Without 3D image registration, it is very hard to find the identical matched slices of the dry specimen and the saturated specimen. Two typical slices with the same height from the sample stage are compared in Figures 2(a) and (b), and their subtraction is listed in Figure 2(d), from which the difference can be clearly distinguished. The 3D data of the dry specimen is registered with that of the saturated specimen, and one typical 2D slice of the registered 3D data corresponding to Figure 2(a) is shown in Figure 2(c). The subtraction between Figures 2(a) and (c) is shown in Figure 2(e), which tells the good match.

3.3 Spatial distribution of local porosity

To calculate the 3D spatial distribution of the porosity using eq. (3), the GSV of water G_w and the GSV of air G_a are required. G_w is read directly from the large pore in tomography images as 0.27 from the CT slice of the saturated specimen, and G_a is read as zero from the dry specimen. After image registration, algebraic operations using eq. (3) can be applied directly to obtain the 3D porosity map, and the results are shown in Figure 3. Figures 3(a), (d), (g) show the 3D porosity maps, Figures 3(b), (e), (h) show the 2D porosity maps, and Figures 3(c), (f), (i) show the line profiles on 2D porosity maps. It is clear that the specimen with larger w/c ratios has lager porosities, as can be seen from the Figures 3(c), (f), and (i). Figures 3(a), (d), and (g) show some macro porosity distributions on the left edge, which might arise from the casting surface. The three specimens are generally homogeneous in macroscale, so no further information can be obtained from the 3D or 2D image maps. The porosity information will be discussed from the probability

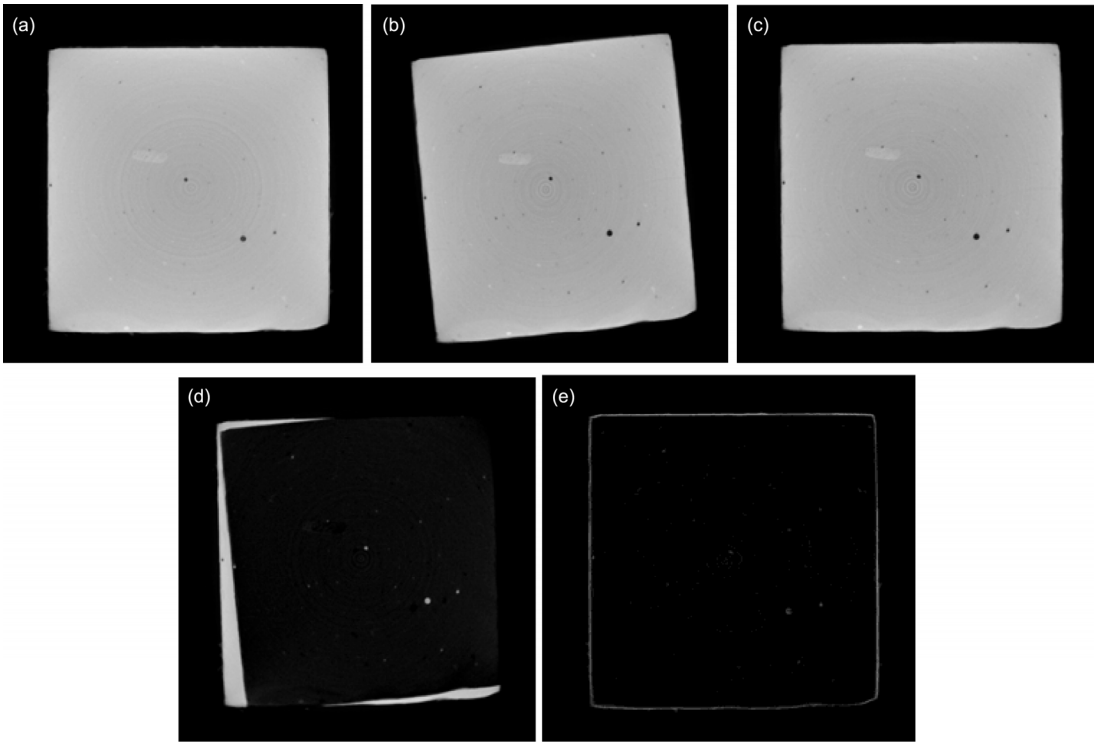

Figure 2 Example slices of P35 specimen showing the image registration results. (a) One typical 2D slice of the specimen at dry state; (b) typical 2D slice of the specimen at the saturated state; (c) the subtraction between (a) and (b); (d) the registered results of (b) based on (a); (e) the subtraction between (a) and (d).

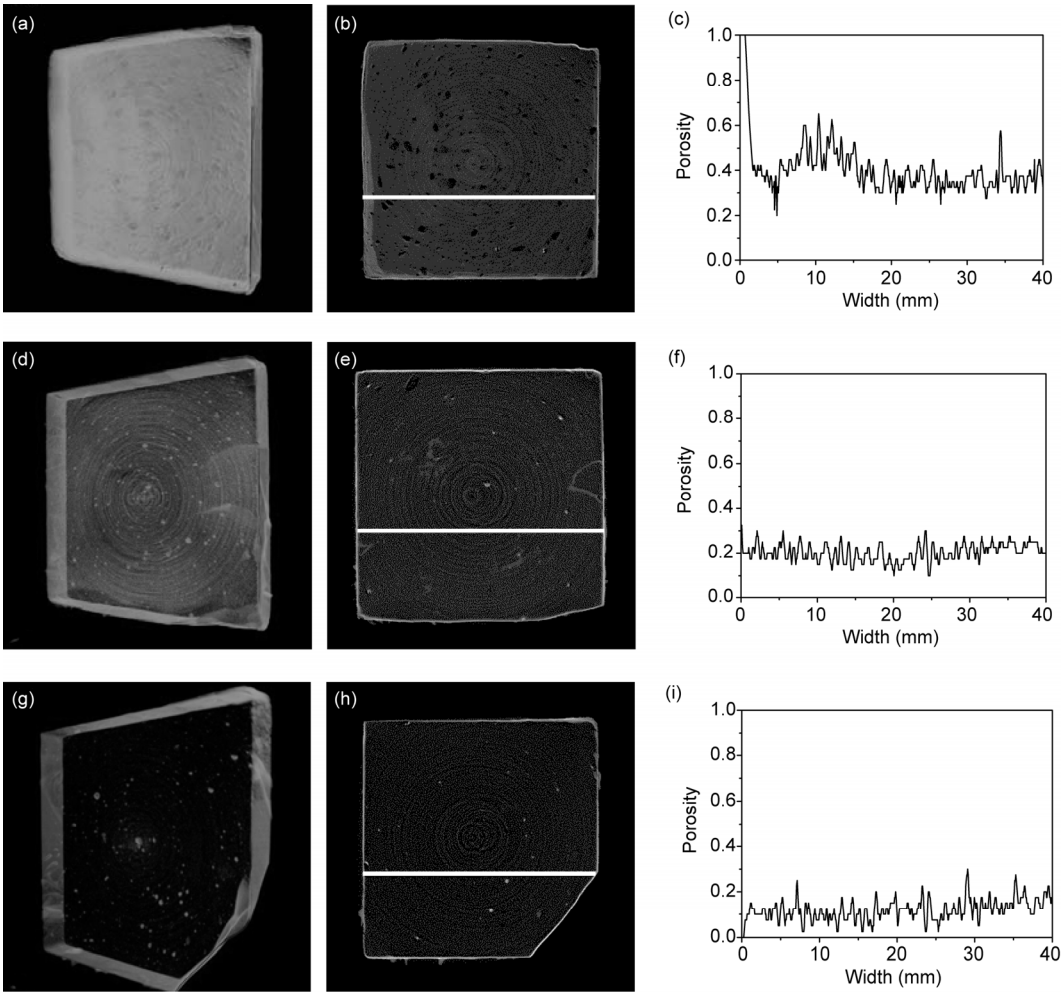

Figure 3 Spatial distribution of local porosity for different specimens. (a), (d), (g) 3D rendering of the porosity map of specimens P53, P35, P23, respectively; (b), (e), (h) typical 2D slice of the porosity map of specimens P53, P35, P23, respectively; (c), (f), (i) 1D porosity distribution of the line in (b), (e), (h), respectively.

view in the next section.

3.4 Local porosity probability

The cement-based materials are heterogeneous in microscale, so the local porosity probability depends on the probe size [24]. When the probe size is small enough, the local porosities will be 0 or 1. When the probe size is large enough, the local porosities will always be the averaged porosity of the whole specimen. In this research, the local porosity probability is evaluated on three different probe sizes, including the RVE size, the smallest probe size, and the characterized size. The smallest probe size l is 60 μm, and the characterized size depends on the RVE size, so the RVE size needs to be determined firstly. Intermediate results in determining the RVE size using average porosities are shown in Figure 4. For each specimen, about 8 points are randomly selected as beginning points, so several curves between the average porosities on different cell sizes and the L size are obtained. All the curves show similar trend from dancing state to stable state. According to the physical meaning of RVE, when the curves become flat enough, the L size is the RVE size. Three dotted lines are drawn in Figure 4 to show where the curves are flat enough, from which the RVE sizes for different specimens can be determined. The characterized size is defined as $L_{\mathrm{RVE}}/5$. The obtained RVE sizes L_{RVE}, the characterized size $L_{\mathrm{RVE}}/5$, and the smallest probe size l are summarized in Table 3.

Although only three w/c ratios were investigated, some rules still can be obtained. It is clearly found that the RVE size decreases with the w/c ratio firstly, and then increases with the w/c ratio. Generally, low w/c ratio corresponds to low hydration degree, and low hydration degree corresponds to low heterogeneity [24], so that the RVE size decreases with the w/c ratio firstly. While when the w/c ratio is quite low (0.23 in this case), the workability is becoming worse, so that the heterogeneity increases again, and then the RVE size increases.

The local porosity probability for three different specimens and on three different probe sizes is shown in Figure 5.

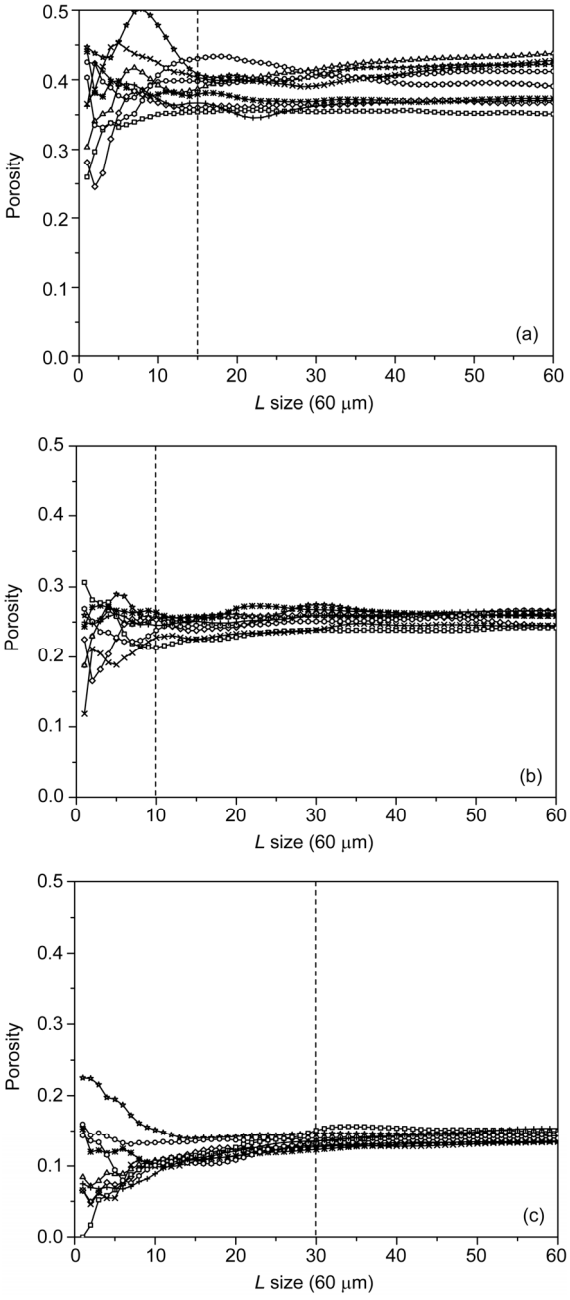

Figure 4 Intermediate results for different specimens in determining the RVE size using average porosities on different volumes, where x-axis is L size and y-axis is the average porosity.

Table 3 Probe sizes used for porosity probability analysis for different specimens

Probe size	P53	P35	P23
L_{RVE} (×60 μm)	15	10	25
$L_{RVE}/5$ (×60 μm)	3	2	5
l (×60 μm)	1	1	1

Some information can be obtained. Firstly, because of the limited spatial resolution, the smallest probe size l (60 μm) is not small enough, so that the statistical histogram shows

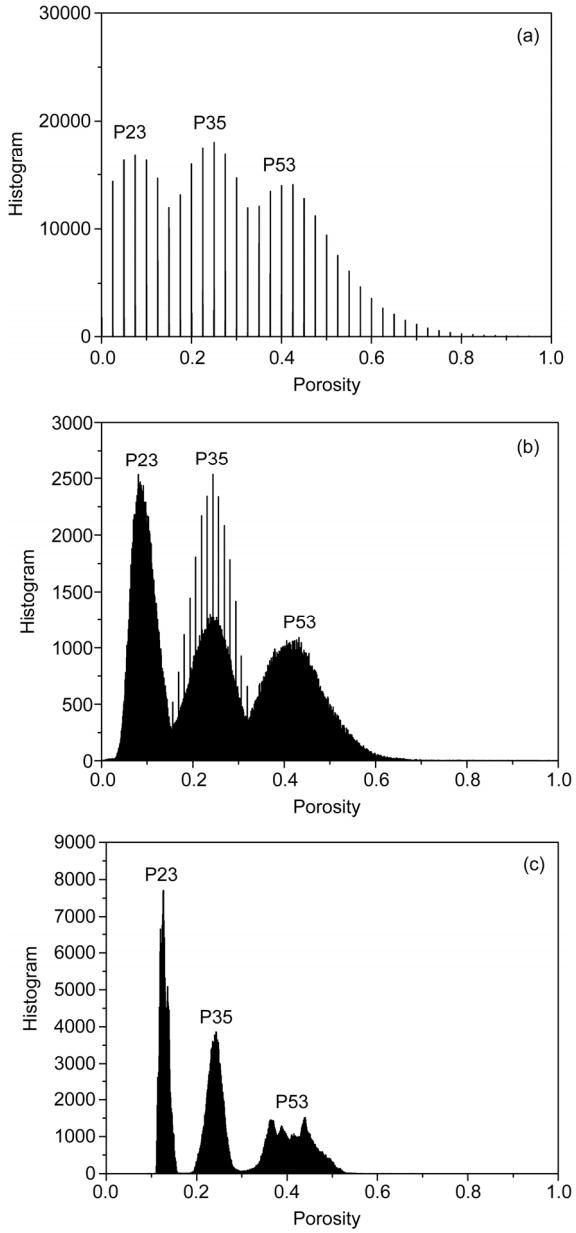

Figure 5 Local porosity probability for different specimens using different probe sizes shown in Table 3. (a) The smallest probe size l; (b) the characterized size $L_{RVE}/5$; (c) RVE sizes L_{RVE}.

only one broad peak around average porosity (peak position of the histogram) for each specimen. Secondly, as expected, the porosity distributions (width of the histogram peak) become narrower when the probe sizes increase. Thirdly, the average porosities (peak position of the histogram) do not depend on probe sizes. Fourthly, the average porosities increase with the w/c ratio for all the three probe sizes. Fifthly, the peak of P53 is not sharp enough at the RVE probe sizes, and further larger probe size does not alter the peak form (not shown here). This might arise from the large bright powders observed on Figure 1. Sixthly, the peak width increases with the w/c ratio from Figures 5(b) and (c), showing the heterogeneity on the characterized probe size and

Table 4 Measured porosities using gravimetric method, MIP method, CT method and the calculated porosity using Powers model for different specimens

Specimen	CT	Gravimetric	MIP	Model-cap	Model-cap+gel
P53	0.41	0.39	0.31	0.23	0.44
P35	0.24	0.27	0.14	0.10	0.32
P23	0.13	0.19	0.09	0.04	0.24

RVE size. The heterogeneity of cement pastes increases with the w/c ratio or hydration degree.

3.5 Average porosity

After 30 months standard curing, maximum hydration degree based on $\alpha = 0.239+0.745 \tanh [3.62(\text{w/c}-0.095)]$ [31] can be supposed. The maximum hydration degree of 0.58, 0.78, and 0.92 are calculated for P53, P35, and P23 respectively. According to Powers model, the capillary porosity and gel porosity can be calculated. The measured porosities using gravimetric method, MIP method, and CT method are compared with the calculated porosities using Powers model [32], all of which are shown in Table 4.

Although with some deviation, the porosities from the CT method and the porosities from gravimetric method show an acceptable match. Both methods are water weighting methods, and this is one kind of verification of the CT method for porosity determination. The MIP porosities are lower than those from the CT method or gravimetric method, and this is reasonable considering that water can enter some gel pores where mercury cannot. Besides, the porosities from the CT method or gravimetric method are larger than the calculated capillary porosities, but lower than the calculated capillary and gel porosities, which implies that some gel pores are still not measured by the water weighting methods.

4 Conclusions

The spatial and frequency distributions of local porosity of cement pastes are characterized with the dual CT scanning methods, which have several advantages. Firstly, compared to the normal image segmentation method, the obtained porosity using the dual CT methods does not depend on the spatial resolution of the imaging systems. Secondly, it can give 3D porosity distribution which is not detectable by the traditional analysis methods. Thirdly, it is nondestructive so that monitoring of porosity evolution on the same specimen is possible. Fourthly, it can be applied to porosity research of all kinds of the cement-based materials, including cement pastes, mortars, and concretes.

The 3D spatial distributions show reasonable heterogeneity for all specimens with the w/c ratios of 0.53, 0.35, and 0.23, and the probability analysis reveals the heterogeneity. The RVE size based on porosity map decreases with the w/c ratio firstly, and then increases with the w/c ratio. Furthermore, the local porosity probability is evaluated on different probe sizes, it is found that the heterogeneity on the characterized probe size or RVE size increases with the w/c ratio or hydration degree.

Besides porosity distributions, average porosities from the current results are also compared with those from the traditional methods. Average porosities obtained using the CT method are consistent with the gravimetric results, however, the values tend to be larger than the corresponding MIP results. Compared with the porosities calculated using Powers model, average porosities using the CT method surpass the calculated capillary porosities and inferior to the sum of the calculated capillary porosities and gel porosities.

This work was supported by the National Natural Science Foundation of China (Grant No. 51008072), the Fundamental Research Funds for the Central Universities (Grant No. 2242014R30014) and State Key Laboratory of High Performance Civil Engineering Materials (Grant No. 2012CEM008).

1 Klobes P, Meyer K, Munro R G. Porosity and specific surface area measurements for solid materials. NIST, Recommended Practice Guide, 2006
2 Taylor H F W. Cement Chemistry. 2nd edit. London: Thomas Telford, 1998
3 Aligizaki K K. Pore Structure of Cement-based Materials: Testing, Interpretation, and Requirements. New York:Taylor Francis, 2006
4 Diamond S. Mercury porosimetry–an inappropriate method for the measurement of pore size distributions in cement-based materials. Cem Conc Res, 2000, 30: 1517–1525
5 Scrivener K L. Backscattered electron imaging of cementitious microstructures: Understanding and quantification. Cem Concr Compos, 2004, 26: 935–945
6 Diamond S. The microstructure of cement paste and concrete–A visual primer. Cem Concr Compos, 2004, 26: 919–933
7 Holzer L, Gasser P, Muench B. Quantification of Capillary Pores and Hadley Grains in Cement Pastes Using Fib-Nanotomography. Proc ECF 16, Greece: Alexandroupolis, 2006
8 Munch B, Holzer L. Contradicting geometrical concepts in pore size analysis attained with electron microscopy and mercury intrusion. J Am Ceram Soc, 2008, 91: 4059–4067
9 Wan K S, Sun W, Tang C K, et al. Three dimensional analysis of micro defect morphologies in cement-based materials using focused ion beam tomography. Sci China Tech Sci, 2012, 55: 1539–1544
10 Landis E N, Petrell A L, Lu S, et al. Examination of pore structure using three-dimensional image analysis of microtomographic data. Concr Sci Eng, 2000, 2: 162–169
11 Bentz D P, Mizell S, Satterfield S, et al. The visible cement data set. J Res Natl Inst Standards Technol, 2002, 107: 137–148
12 Bentz D P, Quenard D A, Kunzel H M, et al. Microstructure and transport properties of porous building materials II: Three-dimensional X-ray tomographic studies. Mater Struct, 2000, 33: 147–153
13 Gallucci E, Scrivener K, Groso A, et al. 3D experimental investigation of the microstructure of cement pastes using synchrotron X-ray microtomography (μCT). Cem Concr Res, 2007, 37: 360–368
14 Sugiyama T, Promentilla M A B, Hitomi T, et al. Application of synchrotron microtomography for pore structure characterization of deteriorated cementitious materials due to leaching. Cem Concr Res, 2010, 40: 1265–1270
15 Ashbridge D A, Thorne M S, Rivers M L, et al. Image optimization and analysis of synchrotron X-ray computed microtomography (CAT)

data. Comput Geosci, 2003, 29: 823–836
16 Sheppard A P, Sok R M, Averdunk H. Techniques for image enhancement and segmentation of tomographic images of porous materials. Phys A, 2004, 339: 145–151
17 Withjack E M. Computed tomography for rock-property determination and fluid-flow visualization. Soc Pet Eng Form Eval, 1988, 3: 696–704
18 Akin S, Demiral M R B, Okandan E. A novel method of porosity measurement utilizing computerized tomography. In Situ, 1996, 20: 347–365
19 Akin S, Kovscek A R. Computed tomography in petroleum engineering research. Geol Soci, London, 2003, 215: 23–38
20 Ketcham R A, Iturrino G J. Nondestructive high-resolution visualization and measurement of anisotropic effective porosity in complex lithologies using high-resolution X-ray computed tomography. Hydrol J, 2005, 302: 92–106
21 Wan KS, Xu Q, Li L, et al. 3D porosity distribution of partly calcium leached cement paste. Constr Build Mater, 2013, 48: 11–15
22 Hilfer R. Geometric and dielectric characterization of porous media. Phys Rve B, 1991, 44: 60–75
23 Biswa B, Manwart C, Hilfer R. Three-dimensional local porosity analysis of porous media. Phys A, 1998, 255: 221–241
24 Hu J, Stroeven P. Local porosity analysis of pore structure in cement paste. Cem Concr Res, 2005, 35: 233–242
25 Hounsfield G N. Computerized transverse axial scanning (tomography), 1, description of system. Brit J Radiol, 1973, 46: 1016–1022
26 Kalender W A. Computed tomography: fundamentals, system technology, image quality, applications. Wiley-VCH Weinheim, 2000
27 Wan K S, Li Y, Sun W. Application of tomography for solid calcium distributions in calcium leaching cement paste. Constr Build Mater, 2012, 36: 913–917
28 Fukuda D, Nara Y, Kobayashi Y, et al. Investigation of self-sealing in high-strength and ultra-low-permeability concrete in water using micro-focus X-ray CT. Cem Concr Res, 2012, 42: 1494–1500
29 Garboczi E J, Bentz D P. The effect of statistical fluctuation, finite size error, and digital resolution on the phase percolation and transport properties of the NIST cement hydration model. Cem Concr Res, 2001, 31: 1501–1514
30 Smilauer V, Bittnar Z. Microstructure-based micromechanical prediction of elastic properties in hydrating cement paste. Cem Concr Res, 2006, 36: 1708–1718
31 Bejaoui S, Bary B. Modeling of the link between microstructure and effective diffusivity of cement pastes using a simplified composite model. Cem Concr Res, 2007, 37: 469–480
32 Hansen T C. Physical structure of hardened cement paste, a classical approach. Mater Struct, 1986, 19: 423–436